applied sciences

MDPI

Article

Fracture-Filling Mechanism of Aluminous Rock Series in the Ordos Basin

Hao Zhao and Jingong Zhang *

Department of Geology, Northwest University, Taibaibei Road No. 229, Xi'an 710069, China; zhao17629135304@163.com
* Correspondence: zhangjg@nwu.edu.cn

Abstract

The "bauxite gas reservoir" in the Ordos Basin represents a novel exploration domain, yet the mechanisms governing its widespread aluminous fracture fillings remain unclear. This study integrates core observation, thin-section analysis, geochemical simulation, and rock physics to investigate the formation and impact of these fracture systems. Results identify a characteristic filling evolutionary sequence of "wall-lining film → oolitic/globular → plug-like → vermicular." Geochemical simulations confirm that increasing *pH* and decreasing *Eh* driven by water–rock interactions are the key drivers for aluminous mineral precipitation. A distinct well log response model characterized by high GR, DEN, and CNL values coupled with low AC and RT is established for effective identification. Seepage experiments reveal that while Al–Si colloidal fracture fillings reduce permeability, they act as natural proppants to preserve effective flow channels, acting as a crucial high-permeability network for gas migration despite the mineral occlusion. These findings refine the accumulation theory for bauxite series reservoirs and provide geological evidence for deep tight gas exploration.

Keywords: Ordos Basin; aluminous rock series; fracture filling; aluminum-related minerals; tight gas; accumulation mechanism

1. Introduction

1.1. Research Background and Scientific Significance

Bauxite and aluminous rocks represent the primary global source of aluminum, a critical industrial metal. Their genesis is inextricably linked to intense surface chemical weathering, leaching processes, and lateritization [1]. Globally, bauxite deposits are classified into two principal types: lateritic and karst. Lateritic bauxites are typically the product of in-situ weathering of aluminosilicate parent rocks [2], preserving the protolith's texture [3]. In contrast, karst-type bauxites are sedimentary deposits accumulated on the paleo-weathering surfaces of carbonate rocks, characterized by complex provenance and multistage mineralization processes [4]. In China, the North China Craton and the Youjiang Basin host large-scale Carboniferous–Permian karst-type bauxite belts, which possess significant mineral economic value and have recently demonstrated immense potential in hydrocarbon exploration [5].

The Ordos Basin, a large multi-cycle superimposed basin in the western North China Craton, contains a widespread suite of coal-bearing strata within the Upper Paleozoic Permian Taiyuan, Shanxi, and Shihezi Formations [6,7]. These strata are not only rich in coal resources but also constitute the basin's main gas source rocks, forming a "total petroleum system" dominated by tight sandstone gas, co-existing with coalbed methane and shale

Check for updates

Academic Editor: Nikolaos Koukouzas

Received: 29 December 2025
Revised: 16 January 2026
Accepted: 17 January 2026
Published: 20 January 2026

Copyright: © 2026 by the authors. Licensee MDPI, Basel, Switzerland. This article is an open access article distributed under the terms and conditions of the Creative Commons Attribution (CC BY) license.

gas. Notably, in the basin's eastern margin and the Longdong area, a bauxite–bauxitic mudstone–aluminous rock series, where "aluminous rock" refers to aluminum-enriched fine-grained clastic rocks formed by intensive leaching and residual enrichment during weathering, is extensively developed overlying the weathering crust of the Lower Paleozoic Majiagou Formation carbonates. For decades, this rock series was regarded as a regional cap rock for tight gas reservoirs [8]. However, recent drilling in the Longdong block and the eastern basin has yielded high-yield industrial gas flows from the bauxite intervals, leading to the emergence of the "bauxite gas reservoir" concept and fundamentally altering traditional views of this stratum [9].

While the macroscopic pore structure and accumulation models of bauxite reservoirs have garnered attention, existing research has largely focused on the bauxite bodies at the stratigraphic scale [10]. There is a paucity of research regarding the secondary enrichment of aluminum-related minerals (e.g., kaolinite, illite, diaspore, and amorphous aluminosilicate gels) within tectonic fracture systems post-deposition and diagenesis [4]. In tight reservoirs, fractures are efficient pathways for fluid migration [11]; their opening, closing, and filling states directly determine gas charging efficiency and single-well productivity [12]. For the aluminous rock series, fractures are not only gas conduits but also sites for formation water leaching and the migration and reprecipitation of aluminum and silicon elements [13]. The minerals filling these fractures act as indicators of the physicochemical properties and migration pathways of paleo-fluids [14].

Therefore, investigating the filling mechanism of aluminum-related minerals in fractures is essential [15]. It helps to reveal the microscopic processes of fluid–rock interaction in the deep basin and provides a scientific basis for evaluating the effectiveness of fractures in tight gas and bauxite gas reservoirs. This article aims to utilize multidisciplinary methods to address the following scientific questions: What are the material sources and precipitation mechanisms of aluminum-related minerals in fractures? How do different filling morphologies indicate the timing of fracture activity and the direction of fluid migration? How does aluminous filling alter the seepage capacity of fractures, and what role does it play in the accumulation process?

1.2. Status of Domestic and International Research

1.2.1. Genesis and Distribution of Bauxite Series

International research on lateritic bauxite is relatively mature, with established metallogenic models based on climate, parent rock, and geomorphological controls [16,17]. For sedimentary (karst-type) bauxite, research focuses on paleogeographic reconstruction and provenance tracing [18,19]. Recently, studies on the Carboniferous–Permian bauxite series in the Ordos Basin have proposed that its parent materials were derived primarily from a mixture of weathering residues of the underlying Ordovician Majiagou Formation carbonates and syn-sedimentary volcanic ash [20–22].

The alteration of these tuffaceous materials is commonly interpreted to involve the chemical weathering of unstable volcanic glass, producing smectite-rich or bentonitic clay precursors, which may subsequently evolve into kaolinite and illite/smectite (I/S) mixed layers during burial diagenesis. These materials underwent intense leaching and desilication during frequent oscillations between marine and continental environments [23], providing the material basis for the development of aluminous mineral assemblages observed in the bauxite series.

1.2.2. Fracture Filling and Fluid Tracing

Fracture mineral filling (veins) is a classic subject in structural geology and fluid geochemistry [24]. Analyzing mineral assemblages (e.g., calcite, quartz, chlorite), micro-

textures (e.g., fibrous, blocky, banded), and fluid inclusions allows for the inversion of paleostress field evolution, as well as changes in fluid temperature, pressure, and composition [4]. However, existing literature mostly focuses on carbonate or siliceous veins [25]. Systematic reports on "aluminous fractures" dominated by aluminum-series minerals like kaolinite, gibbsite, and diaspore are lacking, especially regarding their genetic mechanisms in deep burial environments of hydrocarbon basins [26]. However, aluminous fracture systems fundamentally differ from carbonate and siliceous veins in terms of fluid–rock interaction mechanisms and mineral precipitation pathways. Aluminum exhibits strong hydrolysis behavior and commonly undergoes colloidal and gel-like intermediate stages prior to crystallization, making its precipitation highly sensitive to *pH* and *Eh* evolution rather than simple supersaturation [27]. As a result, fracture fillings dominated by aluminum-series minerals may not act solely as sealing phases, but can exert complex and potentially dual controls on fracture permeability and gas migration [28,29]. These characteristics render existing vein-filling models insufficient for explaining aluminous fracture development in hydrocarbon basins, thereby necessitating a dedicated investigation framework.

1.2.3. Progress in Bauxite Gas Reservoir Exploration

Against this background, since 2020, following breakthroughs in wells such as Long 57 in the Longdong area, research on bauxite gas reservoirs has accelerated [30]. It is confirmed that bauxite possesses high porosity (average 5–10%, locally >20%) and high brittleness, as indicated by its mineralogical composition, enabling it to serve as a high-quality reservoir as well as a cap rock [23]. In log evaluation, typical response characteristics of "high gamma, high density, high neutron" have been summarized, but challenges remain in evaluating fracture effectiveness and quantifying filling degrees [31].

2. Geological Background

2.1. Regional Tectonic Framework

The Ordos Basin is a large intracratonic basin located in the western part of the North China Craton (NCC) and is characterized by long-term subsidence and relatively simple internal structures (Figure 1A) [32,33]. The basin is underlain by a rigid Archean–Paleoproterozoic crystalline basement, which is primarily composed of high-grade metamorphic and igneous rock series, including granulites, TTG (tonalite–trondhjemite–granodiorite) gneisses, amphibolites, and minor metasedimentary supracrustal rocks such as quartzites and marbles. This consolidated basement provided a stable tectonic foundation for the subsequent deposition of thick Paleozoic to Mesozoic sedimentary successions, including the widespread Carboniferous–Permian coal-bearing strata and aluminous rock series, which overlie Ordovician carbonate formations (Figure 1B).

In map view, the basin exhibits an asymmetric rectangular geometry and is bounded by several surrounding orogenic belts, including the Yimeng Uplift to the north, the Weibei Uplift and Qinling Orogen to the south, the Jinxi Flexural Belt and Luliang Mountains to the east, and the Western Thrust Belt together with the Helan–Liupan Mountains to the west. Based on basement properties and deformation characteristics of the sedimentary cover, the basin is subdivided into six first-order tectonic units: the Yimeng Uplift, Weibei Uplift, Jinxi Flexural Belt, Yishan Slope, Tianhuan Depression, and Western Thrust Belt [32].

The study area is mainly located in the transitional zone between the Yimeng Uplift and the Yishan Slope in the northern part of the basin (Figure 1A). Structurally, this region is characterized by a broad and gentle monocline dipping westward, with stratigraphic dips generally less than 1°–2°, reflecting overall tectonic stability (Figure 1C) [34]. Nevertheless, the basin was influenced by far-field effects of multiple tectonic episodes, particularly the Yanshanian and Himalayan movements, which resulted in the development of low-

amplitude nose-like uplifts and associated fault–fracture systems. Although subtle in scale, these micro-structures exert a first-order control on natural gas migration and accumulation. In the northern Yishan Slope, reactivation of basement faults locally induced transtensional fracture systems within the rigid Upper Paleozoic strata, providing favorable space for fluid circulation and late-stage modification of the aluminous rock series [35].

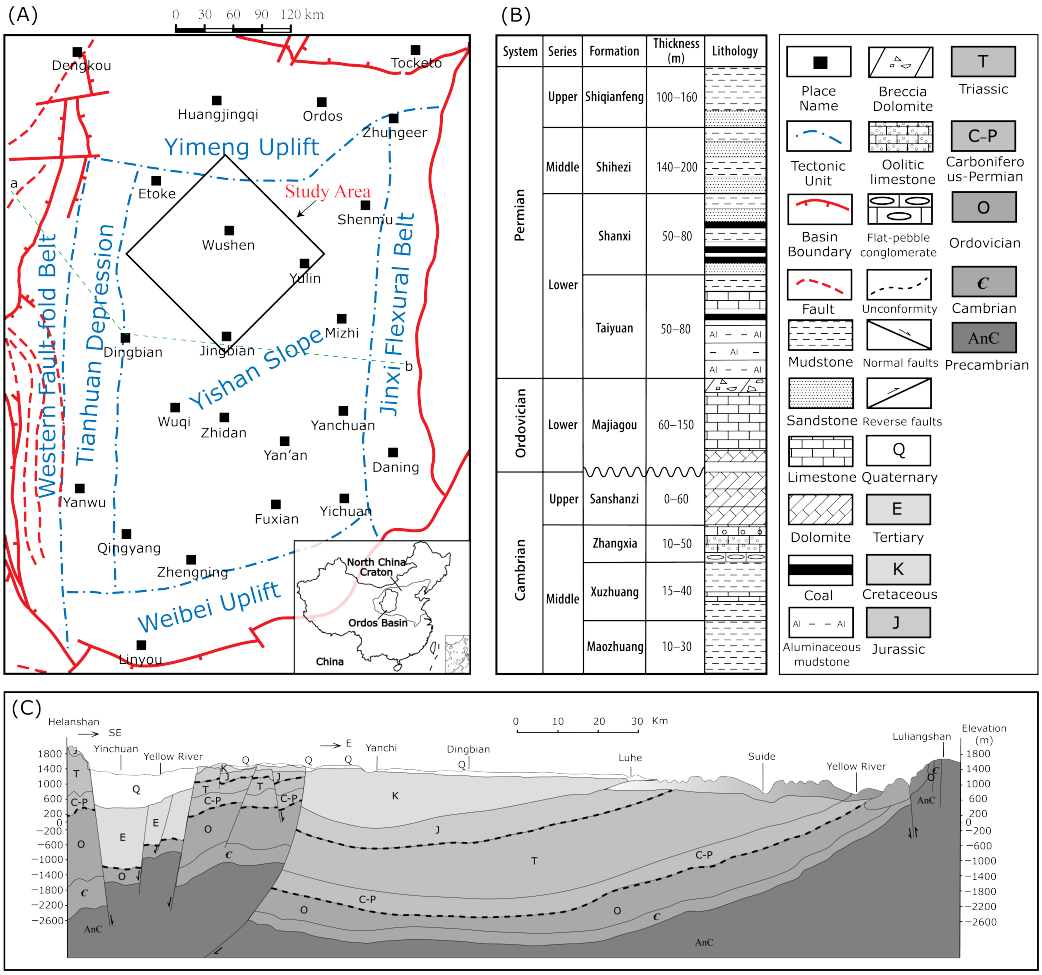


Figure 1. Geological framework and stratigraphic architecture of the Ordos Basin. (**A**) Tectonic subdivision of the Ordos Basin within the North China Craton, showing major structural units and the location of the study area. The green line (a–b) marks the trace of the cross-section in panel (**C**). (**B**) Generalized Paleozoic stratigraphic column of the study area. (**C**) Conceptual west–east geological cross-section along line a–b, illustrating the basin-scale structural style and major stratigraphic successions. The section is schematic and not to scale.

2.2. Stratigraphic Sequence and Characteristics of Aluminous Rock Series

The basin's stratigraphy is well-developed, with outcrops ranging from the Archean basement to the Cenozoic Quaternary [8]. The horizons most relevant to this study are the Lower Paleozoic Ordovician Majiagou Formation and the overlying Upper Paleozoic Carboniferous–Permian strata (Figure 1).

Ordovician Majiagou Formation (O_1m): Composed mainly of thick-bedded dolostone, limestone, and gypsum-salt rocks, serving as the main bedrock for the Paleozoic weathering crust. The Caledonian movement caused the widespread uplift of the North China Platform, subjecting the top of the Majiagou Formation to weathering and denudation for approximately 140 million years. This formed a karst paleogeomorphology with significant relief, including ravines, depressions, and monadnocks, providing depositional sites for bauxitic material enrichment [23].

Carboniferous Benxi Formation (C_2b): Unconformably overlies the Majiagou Formation weathering crust. It consists mainly of a ferro-aluminum rock member, a bauxite rock member, and marine mudstones and limestones. The bauxite series at the base is the core horizon of this study, formed by the in-situ lateritization of bedrock weathering residues and short-distance transport deposition [36].

Permian Taiyuan Formation (P_1t): Conformably overlies the Benxi Formation. It is a marine-continental transitional coal-bearing stratum composed of frequent interbeds of sandstone, mudstone, limestone, and coal seams. The lower part also develops aluminous mudstones and kaolinite clay rocks, constituting the basin's widespread "bauxite series" together with the Benxi Formation.

Permian Shanxi Formation (P_1s) and Shihezi Formation ($P_{1-2}sh$): These are the basin's main gas-bearing layers, dominated by delta plain–front deposits. The organic acid fluids generated by the Shanxi Formation coal measures have a significant impact on the diagenetic evolution of underlying reservoirs [37].

2.3. Fracture Development Background and Fluid Systems

The Upper Paleozoic reservoirs in the study area are typical low-porosity, low-permeability tight reservoirs where fractures are key to improving permeability. Core and imaging logs show that fractures in the area mainly include tectonic fractures, diagenetic fractures, and dissolution fractures [38]. Tectonic fractures are mostly high-angle shear or tensional fractures, striking mainly NE-SW and NW-SE.

Regarding fluid systems, the basin has undergone multistage fluid activities. Early atmospheric freshwater leaching drove the weathering and enrichment of the bauxite series. In the middle stage, coal measures generated hydrocarbons and expelled acids, forming acidic formation waters rich in organic acids and CO_2. These fluids strongly dissolved aluminosilicate minerals like feldspar and rock fragments. In the late stage, massive natural gas charging shifted the fluid environment to a weak acid-neutral, reducing environment [39]. The filling of aluminum-related minerals in fractures is the product of this long-term, multistage fluid–rock interaction.

3. Data Sources and Research Methods

To ensure systemic integrity and reliability, this article employs a comprehensive methodology ranging from macroscopic to microscopic and qualitative observation to quantitative simulation.

3.1. Sample Collection and Data Sources

Physical materials were sourced from the Changqing Oilfield Company, PetroChina, including cores and drilling data from six key exploration wells: Yu 27, Su 76, Su 116, Su 121, Shan 211, and Shan 329. Sampling horizons cover the Permian Shihezi, Shanxi, and Taiyuan Formations, focusing on fractured sandstone, mudstone, and bauxite intervals.

- Core Logging: Detailed descriptions of fractured cores were conducted, recording fracture attitude, density, filling degree, and mineral color.
- Log Data: Complete conventional log curves (GR, DEN, CNL, AC, RT) and partial imaging log data were collected.
- Permeability Data: Provided by the Petroleum Geology Testing Center of the Sinopec Shengli Oilfield Geological Science Research Institute, covering overburden porosity and permeability test data for rock samples with varying fracture-filling degrees.

3.2. Experimental Testing Methods

3.2.1. Polarizing Microscopy and Thin-Section Identification

Thin sections and ordinary thin sections were prepared, with some stained with Alizarin Red to distinguish carbonate minerals. A polarizing microscope (Leica DFC295, Leica Microsystems, Wetzlar, Germany) was used to observe mineral optical characteristics under single plane-polarized light (PPL), cross-polarized light (XPL), and with a λ plate (gypsum plate). Specifically for amorphous/cryptocrystalline aluminosilicate gels, a contrast method was used with standard bauxite thin sections from the Taoqupo outcrop as a reference, identifying them by their low negative relief, full darkness (isotropy), and specific interference colors.

3.2.2. Geochemical Simulation (PHREEQC)

Geochemical simulations were performed using the PHREEQC software (Version 3) to investigate water–rock interactions and aluminous mineral precipitation during fracture filling. All simulations were conducted with the `llnl.dat` thermodynamic database to ensure internal consistency in the treatment of Al-bearing aqueous species and mineral saturation indices [40].

Reaction-path modeling was employed to simulate intermittent interaction between acidic formation water and fracture wall rocks. The initial fluid represents coal-measure acidic water and was defined not only by *pH* but also by major ion composition (Na^+, Cl^-, SO_4^{2-}, and dissolved inorganic carbon), following typical ranges reported for coal-derived formation waters in North China basins [41]. In the simulations, 1 kg of formation water was reacted incrementally with a simplified mineral assemblage dominated by K-feldspar (with minor pyrite), using a stepwise reaction progress (0.05–0.1 mol divided into 100 steps) [42]. This setup corresponds to fluid-limited conditions with a moderate water–rock ratio (on the order of 10^1–10^2), representative of episodic fluid infiltration along fractures under deep burial rather than open-flow systems.

Parameter settings included temperatures ranging from 25 °C to 150 °C, with pressure approximated by hydrostatic conditions. The evolution of *pH* and redox conditions (Eh) was tracked throughout the reaction path, and saturation indices (SI) of key Al–Si colloidal materials, including kaolinite, gibbsite, diaspore, and illite, were calculated at each reaction step [43]. Additional simulations were designed to examine (i) the transition from dissolution-dominated to precipitation-dominated regimes, (ii) temperature-controlled illitization behavior, and (iii) the relative stability fields of amorphous Al–Si colloids versus crystalline gibbsite [44,45]. The simulations are intended to capture relative geochemical evolution trends and mineral precipitation sequences rather than reproduce exact in-situ fluid compositions.

3.2.3. Permeability Stress Sensitivity Testing

The formation overburden conditions were simulated using the CMS-300 overburden pore seepage meter (TerraTek, Salt Lake City, UT, USA). The test steps include:

Pressurization stage: The confining pressure is gradually increased from 2 MPa to 30 MPa. The permeability change is measured, and the fracture closure characteristics are evaluated. Decompression stage: The confining pressure gradually recovers, and the irreversibility of the deformation is evaluated. Compare and analyze the differences in seepage behavior among open fractures, aluminum-filled fractures, and matrix rock samples.

All measured permeability values were retained for statistical analysis, and no outlier filtering was applied.

4. Microscopic Filling Characteristics of Aluminum-Related Minerals in Fractures

Detailed thin-section observations reveal highly complex microscopic structures and filling sequences of aluminum-related minerals in fractures. These features reflect the physicochemical conditions of mineral precipitation and record the dynamic processes of fracture evolution and fluid activity [46]. To provide an independent mineralogical constraint, available X-ray diffraction (XRD) data were also considered, primarily to characterize the bulk and clay–mineral assemblages associated with aluminous fracture systems.

4.1. Typical Mineralogical Characteristics and Identification

In this study, the term "Al–Si colloidal materials" is used as a descriptive petrographic concept referring to optically isotropic to weakly anisotropic, gel-like or cryptocrystalline Al–Si-rich fracture fillings, rather than implying a single, well-defined mineral phase. In the study area, aluminum-related fracture-fill materials mainly include gel-like Al–Si phases (amorphous to poorly crystalline), together with crystalline clay minerals such as kaolinite and illite, and locally diagenetic aluminous phases (e.g., gibbsite- and diaspore/dickite-like minerals) (Figure 2). XRD analyses indicate that the dominant clay–mineral assemblage consists of kaolinite and illite with variable chlorite and illite/smectite mixed layers, providing an independent constraint on the clay–mineral framework (Table 1). However, discrete Al-hydroxide or high-temperature Al-silicate phases inferred from fracture-fill textures are not consistently resolved in bulk XRD patterns, likely due to their low abundance and/or poor crystallinity.

Table 1. Whole rock and clay–mineral X-ray diffraction (XRD) analysis results.

Well	Horizon	Depth (m)	Lithology	Whole Rock Comp. (%)			Clay–Mineral Comp. (Relative %)			
				Qtz	Cal	Total Clay	Ill	Kao	Chl	I/S
Su 76	Shan-22	3217.60	Sandstone	60	–	40	39	43	8	10
Su 116	Upper He-8	3514.85	Sandstone	92	–	8	58	12	30	–
Shaan 329	Lower He-8	3697.80	Sandstone	92	–	8	13	35	41	11
Shaan 256	He-7	3215.80	Sandstone	91	–	9	23	21	54	2
Shaan 211	Lower He-8	2854.30	Sandstone	83	7	10	29	25	46	–
Mi 11	Shan-1	2038.59	Sandstone	93	–	7	54	21	11	14
Mi 11	Shan-1	2041.70	Sandstone	93	–	7	49	20	25	6
Mi 11	Shan-1	2036.48	Sandstone	83	–	17	76	11	13	–

Note: Qtz = Quartz; Cal = Calcite; Ill = illite; Kao = kaolinite; Chl = Chlorite; I/S = illite/smectite mixed layer. "–" indicates below detection limit.

Colloidal Al–Si Materials (Gel-like to Poorly Crystalline)

This material represents the most characteristic early-stage filling observed in fractures.

- PPL characteristics: Colorless and transparent, lacking a fixed crystal form, commonly appearing as flowing, banded, or globular aggregates. The material exhibits low negative relief (refractive index < 1.48) and a smooth, homogeneous surface.
- XPL characteristics: Predominantly extinct or displaying extremely low-order interference colors. Rotation of the stage through 360° produces minimal brightness variation, indicating isotropic to very weakly anisotropic behavior consistent with amorphous to cryptocrystalline materials [36].

- λ-plate response: Upon insertion of the gypsum plate, the material shows a uniform pink to purple-red first-order interference color without discernible lattice orientation. This response differs markedly from well-crystallized quartz or calcite and is consistent with gel-like or poorly crystalline Al–Si materials enriched in structural water [47].

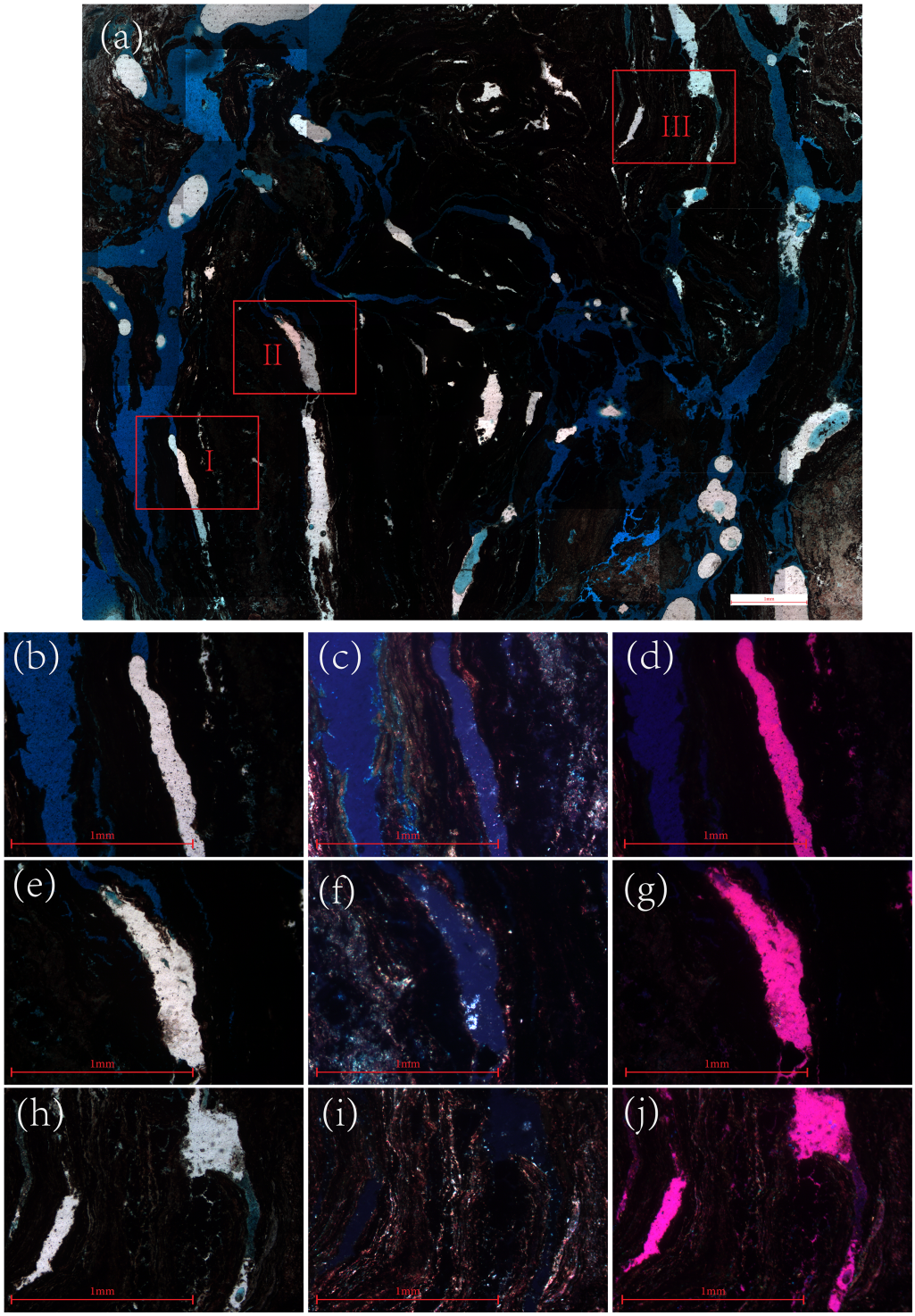


Figure 2. Observation of bauxite thin sections in Taoqupo showing typical gel-like aluminous fracture fillings. (**a**) Splicing diagram of bauxite thin sections in the Taoqupo section; (**b**–**d**) PPL, XPL, and XPL with λ plate images of Al–Si colloidal materials in area I; (**e**–**g**) corresponding images in area II; (**h**–**j**) corresponding images in area III. The consistent optical responses under PPL, XPL, and λ plate indicate the presence of amorphous to poorly crystalline Al–Si gel-like materials lining and filling fractures.

Figure 2 integrates PPL, XPL, and λ-plate observations from multiple fracture domains and reveals a consistent set of optical characteristics for the early-stage Al–Si colloidal fracture fillings. The absence of fixed crystal morphology under PPL, the near-complete extinction under XPL, and the uniform first-order interference colors under the λ plate collectively indicate that these materials lack long-range crystallographic order. Such optical behavior is characteristic of Al–Si colloidal materials (gel-like to cryptocrystalline) rather than well-crystallized aluminosilicate minerals. The recurrence of these features across different fracture areas suggests that gel-like precipitation represents a common and systematic early filling process, providing direct petrographic support for the proposed initial stage of the fracture-filling sequence.

It should be emphasized that optical microscopy alone cannot unambiguously distinguish truly amorphous Al–Si gel from extremely fine-grained cryptocrystalline aggregates. Therefore, the identification of this early-stage fracture-fill material is based on integrated optical characteristics, textural context, and thermodynamic constraints, and the associated uncertainty is acknowledged.

4.2. Filling Micro-Structures and Fluid Migration Indicators

Fracture fillings are not uniformly distributed but instead display characteristic geometric morphologies controlled by crack-seal mechanisms and fluid dynamics (Figures 2–5).

4.2.1. Wall-Lining Film Structure

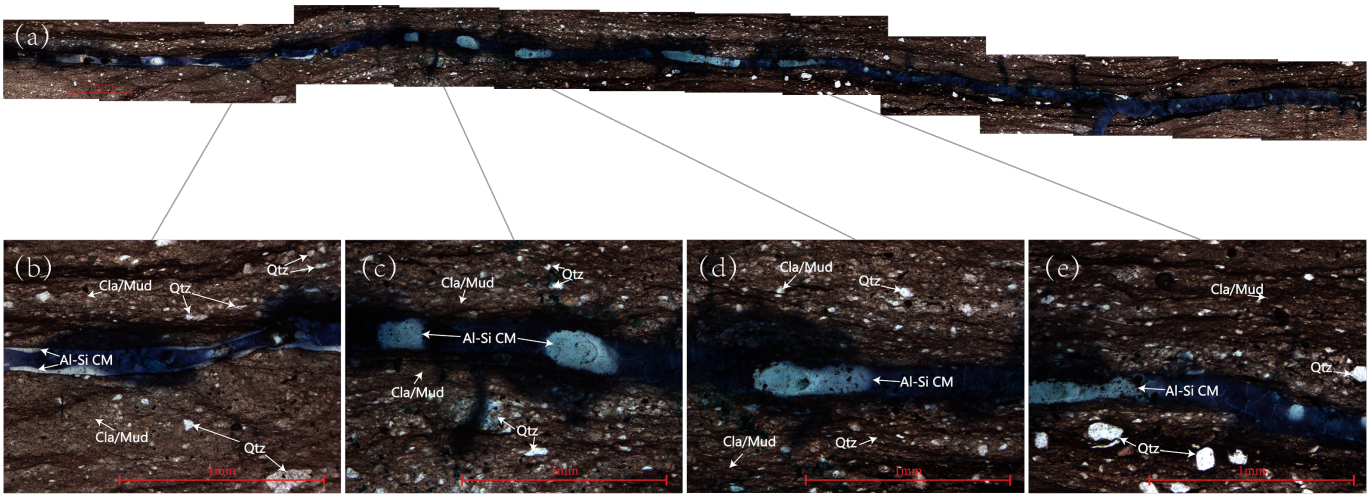
In mudstone fractures from Well Shan 211 (Figure 3), Al–Si colloidal materials occur as continuous thin films coating the fracture walls. Film thickness may taper or thicken along the fracture length, reflecting spatial variations in fluid supply. Based on crystal growth patterns and fluid–rock interaction relationships, the growth direction of these films commonly points toward the fracture center or fluid source [48]. This texture indicates rapid nucleation and adsorption-controlled precipitation during the initial fracture-opening stage, when fluid velocity was relatively high and dissolved species preferentially accumulated along fracture walls [49].

4.2.2. Plug-like (Meniscus) Structure

Thin sections from Well Su 76 (Figure 4) show fractures partially occupied by fusiform or short-columnar colloidal plugs, with unfilled voids or later cements preserved between individual plugs. These plug-like fillings are interpreted to form under gas–water two-phase flow conditions. Under unsaturated states, capillary forces promote the development of localized liquid bridges within fractures, which subsequently undergo precipitation during evaporation or water–rock interaction. The accumulation of multiple discrete plugs significantly reduces fracture connectivity, segmenting originally continuous flow pathways into isolated pore units and thereby enhancing the sealing capacity of the fracture system [48].

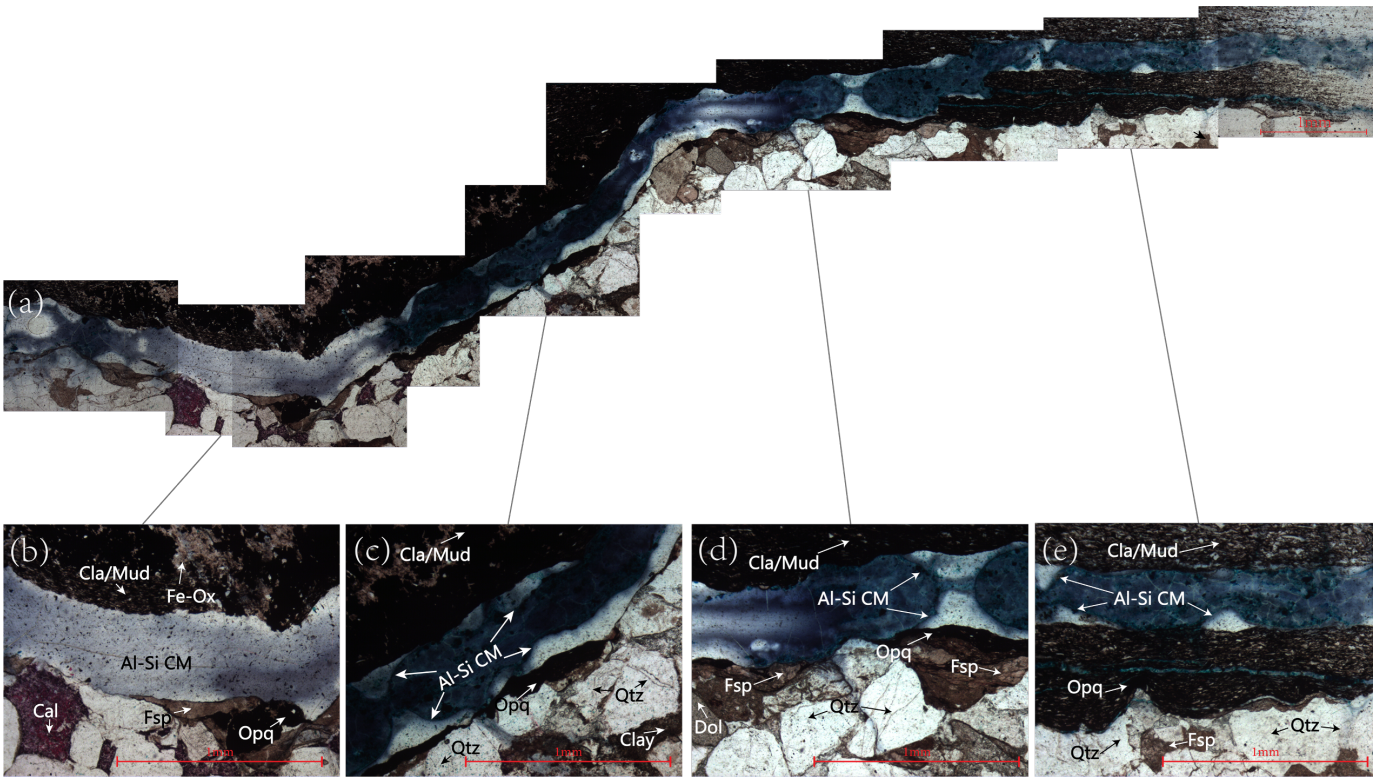
4.2.3. Oolitic-like and Globular Textures

Al–Si colloidal materials aggregate into globular to elliptical bodies, forming oolitic-like textures in a purely morphological sense. In sandstone fractures from Well Yu 27 (Figure 5), Al–Si colloidal materials aggregate into globular to elliptical bodies that are locally arranged in a bead-like pattern along the fracture axis. Representative globular aggregates are directly identified and labeled in the thin-section images.



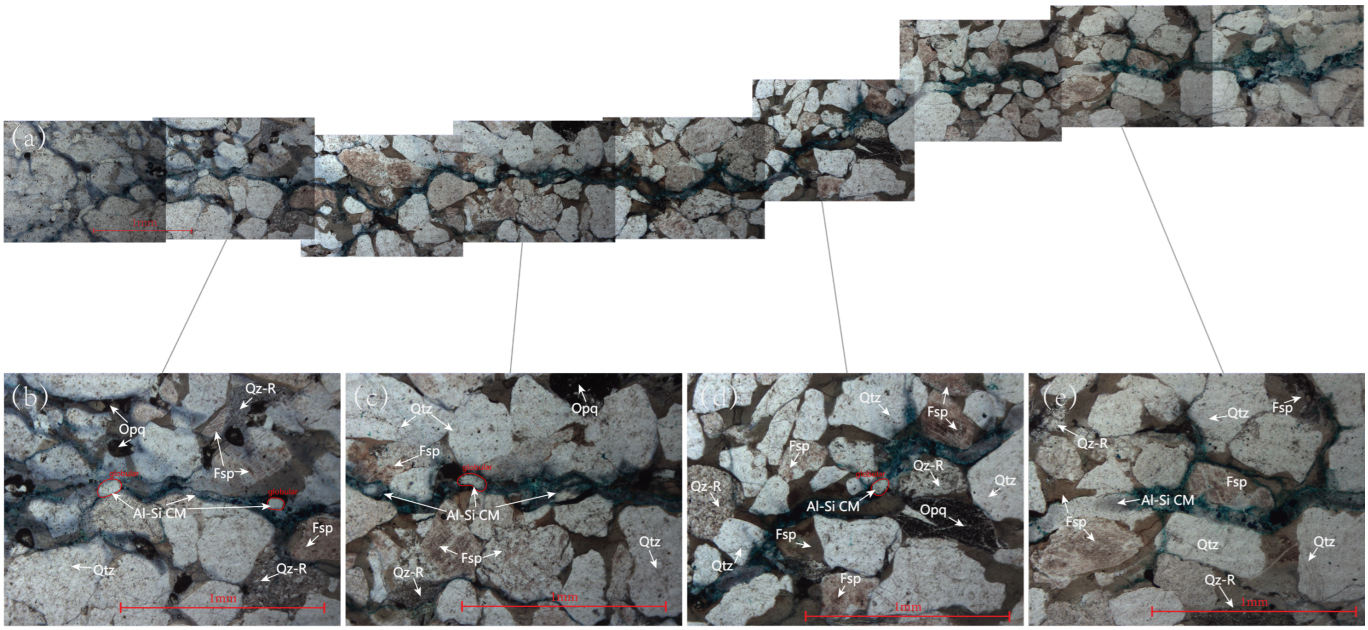
Note: Al-Si CM = aluminum-silicon colloidal materials, Qtz = quartz, Cla/Mud = clay minerals/mudstone marix

Figure 3. Thin-section images of mudstone fractures from Well Shan 211 at a depth of 2921.1 m. (**a**) Overview of mudstone and fracture geometry; (**b**) wall-lining aluminous film coating fracture surfaces; (**c**) locally thickened aluminous accumulations; (**d**) segmented fracture fillings; (**e**) worm-like residual pore structures between fillings.



Note: Al-Si CM = aluminum-silicon colloidal materials, Qtz = quartz, Fsp = feldspar, Cla/Mud = clay minerals/mudstone marix, Opq = opaque minerals, Fe-Ox = iron oxids, Cal = calcite, Dol = dolomite,

Figure 4. Thin-section images of fractures from Well Su 76 at a depth of 3152.36 m. (**a**) Sand–mudstone interface with fracture development; (**b**) fusiform and short-columnar aluminous plugs partially occupying the fracture; (**c**–**e**) wall-adhering Al–Si colloidal materials and residual voids preserved between individual plugs.



Note: Al-Si CM = aluminum-silicon colloidal materials, Qtz = quartz, Fsp = feldspar, Opq = opaque minerals, Qz-R = quartzite rock fragment

Figure 5. Thin-section images of sandstone fractures from Well Yu 27 at a depth of 2287.8 m (Shihezi Formation). (**a**) Overview of sandstone host rock and fracture geometry; (**b**) beaded arrangement of ellipsoidal Al–Si colloidal aggregates along the fracture axis; (**c**) locally segmented accumulations of Al–Si colloidal materials; (**d**) asymmetric colloidal bodies showing rounded upstream and tapered downstream morphology; (**e**) residual pore space and worm-like voids between aggregated fillings.

These aggregates commonly display asymmetric deformation, characterized by a rounded upstream margin and a tapered downstream tail. According to fluid-mechanical principles, such "round-head–pointed-tail" morphologies can be used to infer the paleoflow direction of fracture-hosted fluids [50]. This texture indicates pulsating flow conditions within the fracture, under which colloidal flocculation and gravitational settling preferentially occur in zones of reduced flow velocity.

4.2.4. Vermicular Texture

In extremely narrow fracture tips or compacted channels, Al–Si colloidal materials appear as slender, curved filaments or worm-like shapes. This results from the plastic flow of high-viscosity Al–Si colloidal materials under shear stress. The vermicular extension direction often indicates the residual fluid expulsion direction during fracture closure.

4.3. Paragenetic Sequence

Based on the characteristics of cores and thin sections from each well, this study proposes a four-stage evolutionary model for aluminous fracture filling as a generalized framework to interpret fracture-filling histories (Figure 6). The schematic diagram illustrates the progressive transition from open fractures to fully sealed systems under evolving fluid–rock interaction conditions.

Level 0 (initiation stage): fracture formation and injection of acidic fluids, with no mineral filling and high fracture conductivity.

Level I (film formation stage): the infiltrating fluid reacts with the surrounding rock, resulting in a gradual increase in *pH*. Aluminous colloids form and develop micron-scale adherent films on fracture wall surfaces.

Level II (agglomeration stage): with decreasing flow velocity, colloidal particles flocculate to form bean-like or globular aggregates, which may settle under gravity or preferentially accumulate in locally constricted fracture segments, producing bead-like fillings.

Level III (segmental plug or blockage stage): the filling material continues to grow and coalesce, forming discontinuous or segmental plugs that partially block the main fracture conduit, while residual fluids migrate through remaining pathways and generate worm-like textures.

Level IV (diagenetic transformation stage): under deep burial conditions, increasing temperature promotes dehydration and crystallization of aluminous colloids, leading to transformation into crystalline phases such as diaspore and illite. At this stage, fractures are largely healed, with only intergranular micropores locally preserved (Figure 6).

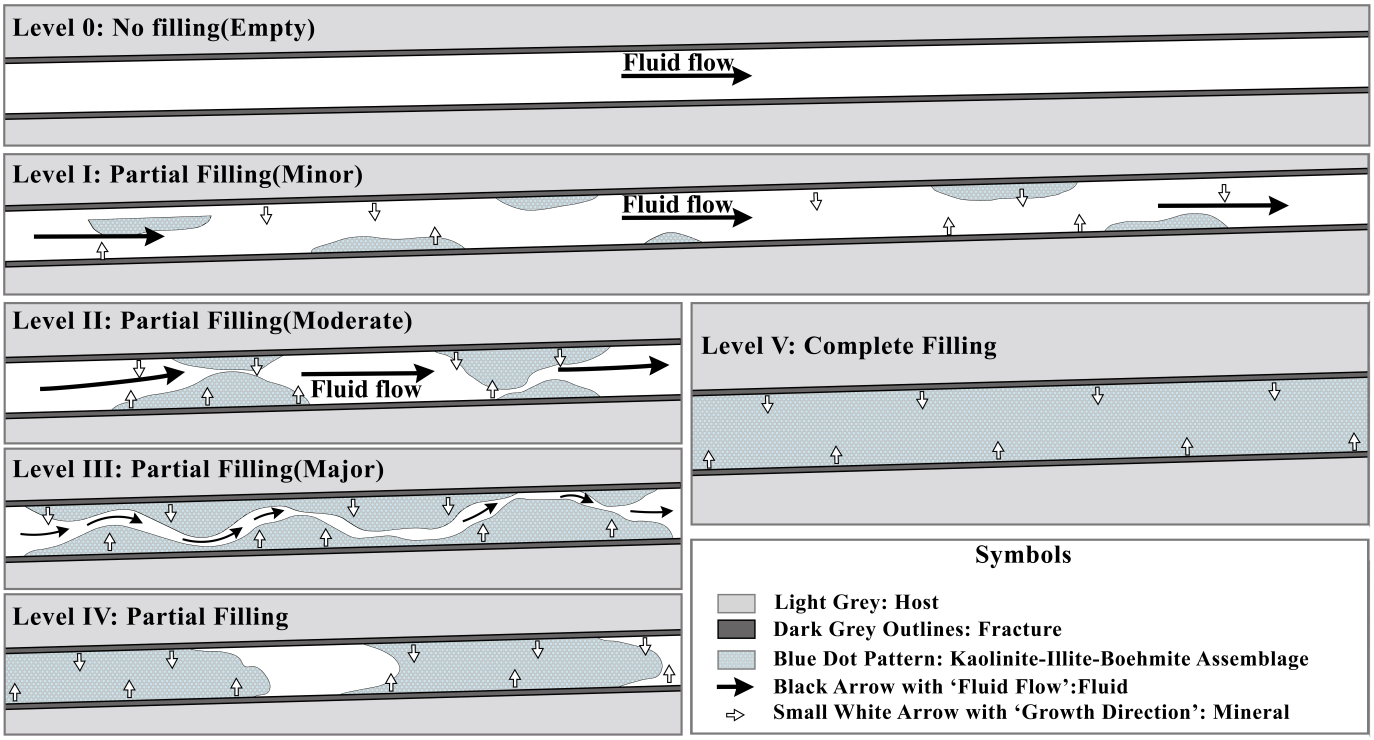


Figure 6. Schematic diagram illustrating the four-stage evolutionary model of aluminous fracture filling. The model depicts the progressive transition from open fractures with high conductivity (Level 0), through wall-lining film formation (Level I), colloidal agglomeration and bead-like accumulation (Level II), segmental plug development and partial blockage (Level III), to late-stage diagenetic crystallization and fracture healing under deep burial conditions (Level IV).

These fracture-filling stages can be broadly linked to the tectonic evolution of the basin, with fracture initiation and early film-like fillings corresponding to Late Paleozoic–Early Mesozoic extensional to transtensional regimes, and later plug formation and diagenetic transformation associated with progressive burial and post-Yanshanian tectonic quiescence.

It should be emphasized that the proposed four-stage model represents a dominant and idealized evolutionary pathway derived from the most representative petrographic features observed in the studied samples. In natural fracture systems, mineral filling processes are not necessarily strictly linear and may exhibit localized deviations, including partial overprinting between stages, episodic precipitation events, or minor textural reworking within individual fractures.

In the present dataset, no systematic evidence for large-scale retrograde dissolution or fully cyclic filling sequences was identified. However, local textural variations suggest that mineral precipitation could occur intermittently, resulting in transitional features between adjacent stages. Such complexity reflects the inherent heterogeneity of fracture-controlled fluid–rock interactions under deep burial conditions and does not invalidate the proposed

stage-based framework, which is intended to capture the principal evolutionary trend of aluminous fracture filling.

4.4. Tectonic Implications for Fracture Development and Infill Chronology

Although the fracture analysis presented in this study is primarily based on core-scale observations, the observed fracture types can be reasonably linked to different tectonic stages to establish a relative framework for fracture-filling chronology. Opening-mode fractures characterized by planar geometries and limited shear displacement are interpreted to have formed during extensional or stress-release stages, providing effective pathways for early fluid infiltration. These fractures are commonly associated with early-stage wall-lining films and gel-like aluminous precipitates, suggesting that initial filling occurred shortly after fracture opening.

In contrast, fractures exhibiting segmentation, necking, or partial closure are more consistent with subsequent stress reorganization during burial or compressional stages. Such fractures preferentially host agglomerated, plug-like, or crystalline Al–Si colloidal fracture fillings, indicating progressive sealing during later deformation and diagenetic modification. This systematic relationship between fracture type, inferred tectonic stage, and filling style provides a strengthened relative temporal framework for interpreting the infill chronology.

5. Geochemical Simulation and Genetic Mechanism

To quantitatively reveal the physicochemical conditions of aluminous mineral precipitation, PHREEQC was used to simulate the "formation water–feldspar/mudstone" reaction path [51].

5.1. Reaction Path and Fluid Property Evolution

Initial geochemical conditions were set to simulate coal-measure acidic formation water [52], with a temperature of 60 °C, an initial *pH* of 4.0, and a representative mineral assemblage consisting of K-feldspar, kaolinite, and quartz [53]. This assemblage reflects common aluminosilicate components in coal-bearing strata and provides a basis for evaluating fluid–rock interactions during early fracture infiltration.

As the reaction proceeds, dissolution of K-feldspar plays a key role in controlling the coupled evolution of *pH* and *Eh*. The dominant reaction can be expressed as:

$$2KAlSi_3O_8 + 2H^+ + 9H_2O \rightarrow Al_2Si_2O_5(OH)_4 + 4H_4SiO_4 + 2K^+$$

This reaction explicitly consumes hydrogen ions, leading to a rapid increase in solution *pH* as feldspar dissolution progresses [54]. The simulation results indicate that *pH* rises from the initial acidic condition (*pH* 4.0) to weakly alkaline values of approximately 6.5–7.5. Under the closed-system assumption adopted in the model, progressive consumption of oxidizing species during water–rock interaction further drives a decrease in redox potential (*Eh*) [26], shifting the system from relatively oxidizing to moderately reducing conditions [50].

The coupled increase in *pH* and decrease in *Eh* establishes a weakly alkaline, reducing geochemical environment (Figure 7), which is favorable for the destabilization of dissolved Al species and subsequent precipitation of aluminous colloids [45]. These results provide a thermodynamic basis for the early-stage formation of gel-like aluminous fracture fillings observed in thin sections.

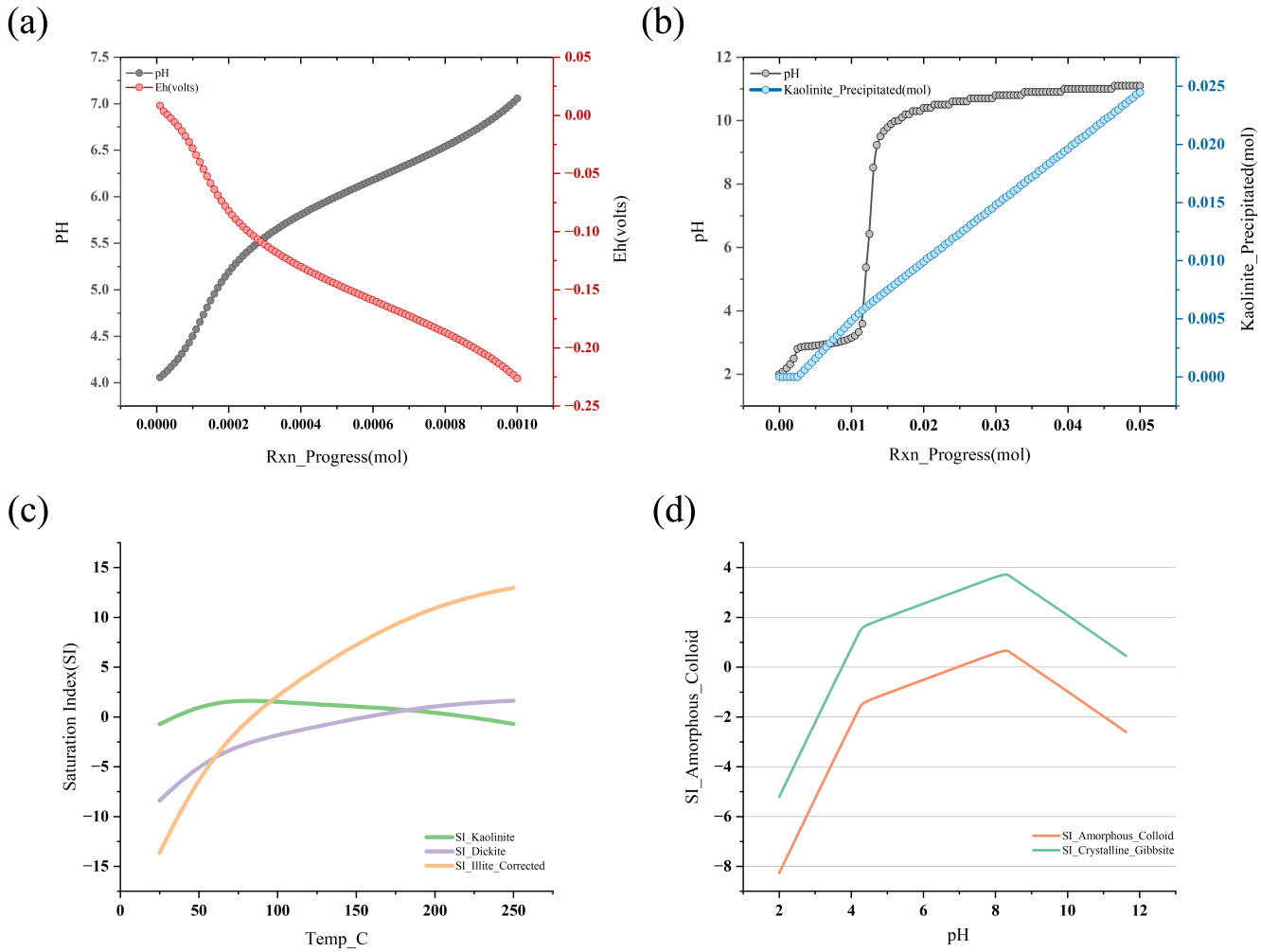


Figure 7. (**a**) *pH*−*Eh* intersection diagram; (**b**) *pH* and kaolinite precipitation diagram; (**c**) Stability domain diagram of kaolinite−illite−ground stone; (**d**) Stable domain diagram of aluminum colloidal minerals. Panels (**a**–**d**) correspond to reaction progress, precipitation amount, temperature-dependent SI, and *pH*-dependent stability fields, respectively.

5.2. Thermodynamic Window of Mineral Precipitation

Stability of kaolinite: Early in the reaction (*pH* 4.0–6.0), kaolinite's saturation index (SI) increases rapidly and stays >0, making it the main precipitate in acidic environments. Simulated precipitation increases linearly with *pH*, peaking around *pH* 6.0 (Figure 7b).

Formation of Aluminum Colloid/Gibbsite: When *pH* rises to neutral (6.5–8.0), aluminum solubility is minimal. If solution Al^{3+} is high, amorphous $Al(OH)_3$ (Gibbsite precursor) forms easily [55]. Simulation shows gibbsite enters the supersaturated zone at *pH* > 6.0. This explains why fractures often show early kaolinite coated by late colloidal Al–Si colloidal materials.

5.3. Temperature Control on Mineral Transformation

To evaluate the influence of burial heating on aluminous mineral stability, temperature sensitivity simulations were conducted over a range of 25–150 °C under otherwise identical geochemical conditions. The results reveal a systematic, temperature-dependent shift in mineral stability that is closely linked to the coupled evolution of *pH*, *Eh*, and mineral saturation states (Figure 7).

As shown in Figure 7a, progressive water–rock interaction during feldspar dissolution leads to a concurrent increase in *pH* and decrease in *Eh*, establishing a weakly alkaline

and reducing geochemical environment. This chemical evolution provides the prerequisite conditions for aluminous mineral precipitation and subsequent phase transformation during burial.

The relationship between *pH* evolution and early aluminous mineral precipitation is illustrated in Figure 7b. Kaolinite precipitation initiates once *pH* increases beyond acidic conditions and continues steadily with reaction progress, indicating that early-stage fracture fillings dominated by gel-like or weakly crystalline Al–Si colloidal materials are closely associated with fluid alkalization driven by water–rock interaction.

The temperature-dependent stability of Al–Si colloidal materials is further constrained by saturation index (SI) calculations; see Figure 7c. At relatively low temperatures (<80 °C), kaolinite and gibbsite exhibit near-saturated to supersaturated conditions, indicating thermodynamic stability and favoring their precipitation. With increasing temperature (>120 °C), the SI values of kaolinite and gibbsite progressively decrease, whereas those of diaspore (AlO(OH)) and illite increase markedly. This trend reflects the enhanced stability of more dehydrated and structurally ordered aluminous phases under elevated burial temperatures. The corresponding long-term diagenetic tendency can be schematically expressed as:

$$Al_2Si_2O_5(OH)_4\ (\text{kaolinite}) + 2K^+ \xrightarrow{T\uparrow} K\text{-bearing illite} + SiO_2 + H_2O$$

Importantly, this reaction represents a thermodynamic evolution trend rather than an instantaneous mineral replacement, capturing the progressive transformation of kaolinite-group minerals toward illite and diaspore during burial heating.

The contrasting stability fields of amorphous versus crystalline aluminous phases are highlighted in Figure 7d. Amorphous aluminous colloids exhibit maximum stability at intermediate *pH* values but become progressively destabilized at higher *pH*, whereas crystalline gibbsite maintains a broader supersaturation range. This contrast indicates that early gel-like aluminous precipitates likely form under metastable conditions and may subsequently dehydrate and recrystallize into more stable crystalline phases as fluid chemistry and temperature evolve.

The geochemical simulations presented in this study are based on equilibrium thermodynamic calculations, which are appropriate for evaluating stability fields and relative precipitation sequences but do not explicitly resolve reaction kinetics. In natural fracture systems, the precipitation of aluminiferous gels is likely influenced by kinetic factors such as nucleation barriers, polymerization rates, and fluid residence time. Consequently, early-stage gel-like Al–Si phases may persist beyond their predicted equilibrium stability fields. Therefore, the simulation results are interpreted as indicators of relative thermodynamic driving forces and evolutionary tendencies rather than instantaneous precipitation behavior. This distinction does not affect the proposed fracture-filling sequence but highlights the complementary roles of thermodynamics and kinetics in controlling aluminous fracture filling.

6. Well Log Response Characteristics and Identification Model

Establishing wellbore-scale identification methods is crucial. Based on core-to-log calibration, the geophysical response of aluminous fracture-filling zones is summarized [56].

6.1. "Three Highs and Two Lows" Log Response

Statistics from wells Yu 27, Su 76, and other representative wells demonstrate that intervals (Figure 8) with confirmed aluminous fractures exhibit a consistent and diagnostic log response pattern (Table 2). Specifically, aluminous fracture zones are characterized by

high natural gamma (GR), high bulk density (DEN), and elevated neutron porosity (CNL), coupled with low acoustic transit time (AC) and low resistivity (RT), forming a distinctive "three-high and two-low" logging signature.

The elevated GR values reflect enrichment of radioactive elements (Th and U) associated with aluminous and clay-rich materials, while the high-density response is controlled by the intrinsically high densities of aluminum-bearing minerals and the compact nature of fracture fillings. Increased CNL values are primarily attributed to bound and structural water within clay minerals and gibbsite, rather than effective pore space. In contrast, the reduced AC values indicate a stiffened rock framework due to fracture healing, and the low resistivity response reflects the combined effects of microporosity, bound water, and the high cation exchange capacity of clay-rich fillings.

Together, these coupled log responses provide a robust physical basis for identifying aluminous fracture-filling zones and distinguish them from other high-gamma lithologies when multiple logs are evaluated jointly.

Table 2. Statistical characteristics and physical interpretation of log responses in aluminous fracture-filling zones.

Log Curve	Symbol	Unit	Typical Range	Physical Mechanism
Natural Gamma	GR	API	120–200	Bauxite series enriches radioactive elements (Th, U); strong clay adsorption capabilities.
Bulk Density	DEN	g/cm^3	2.55–2.75	High density of aluminum minerals (Diaspore ≈ 3.4, kaolinite ≈ 2.6) and dense filling structures.
Neutron Porosity	CNL	p.u.	15–25	High neutron deceleration caused by crystal/bound water in clay/gibbsite; does not reflect effective porosity.
Acoustic Time	AC	μs/m	190–220	Low transit time (high velocity) reflects a hard skeleton and healed fractures.
Resistivity	RT	Ω · m	1–20	Low resistivity due to micropores, bound water, and high cation exchange capacity of clay.

6.2. Multi-Parameter Crossplot Identification

Based on these differences, GR–DEN and GR–AC crossplots were constructed (Figure 9) to further evaluate the logging response characteristics of aluminous fracture zones and to reduce potential lithological ambiguity.

In the GR–DEN crossplot, aluminous fracture intervals cluster predominantly in the upper-right quadrant, characterized by high GR and high density, forming a distinct "aluminous filling island" [31]. This feature contrasts with organic-rich shales, which may exhibit high GR values but typically show lower density due to elevated organic matter content.

In the GR–AC crossplot, aluminous fracture points are concentrated in the lower-right quadrant (high GR and low AC), reflecting the combined effects of dense Al–Si colloidal fracture fillings and fracture-controlled fluid pathways. In comparison, volcanic ash or tuffaceous layers, although locally associated with high GR, generally display different density–neutron–acoustic coupling patterns and do not form a consistent low-AC cluster.

As illustrated by the clustering behavior in Figure 9, aluminous fracture zones occupy a relatively discrete parameter space that can be effectively distinguished from shale- and ash-dominated lithologies when multiple logs are considered jointly. Using this crossplot-based diagnostic approach, multiple aluminous fracture zones (0.5–2 m thick) were successfully identified in blind tests of Wells Su 116 and Su 121 and subsequently confirmed by core observations [31].

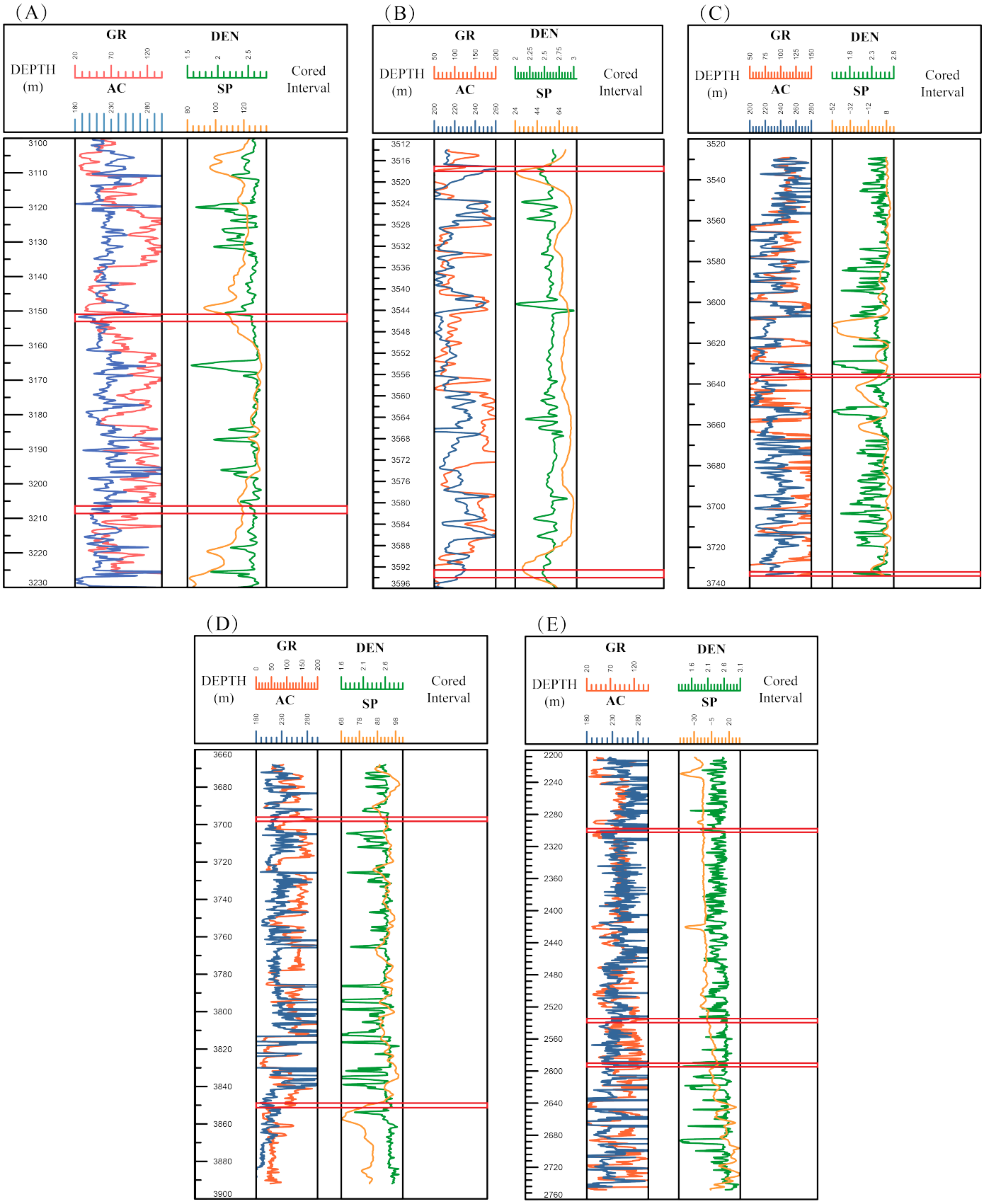


Figure 8. Logging curve of the study area (**A**) Logging curve of Well Su76 and its core sampling section; (**B**) Logging curve and core sampling section of Well Su 116; (**C**) Logging curve and core sampling section of Well Su 121; (**D**) Logging curve and core sampling section of Well Shaanxi 329; (**E**) Logging curve and core sampling section of Well Yu 27; Red box indicate coring locations.

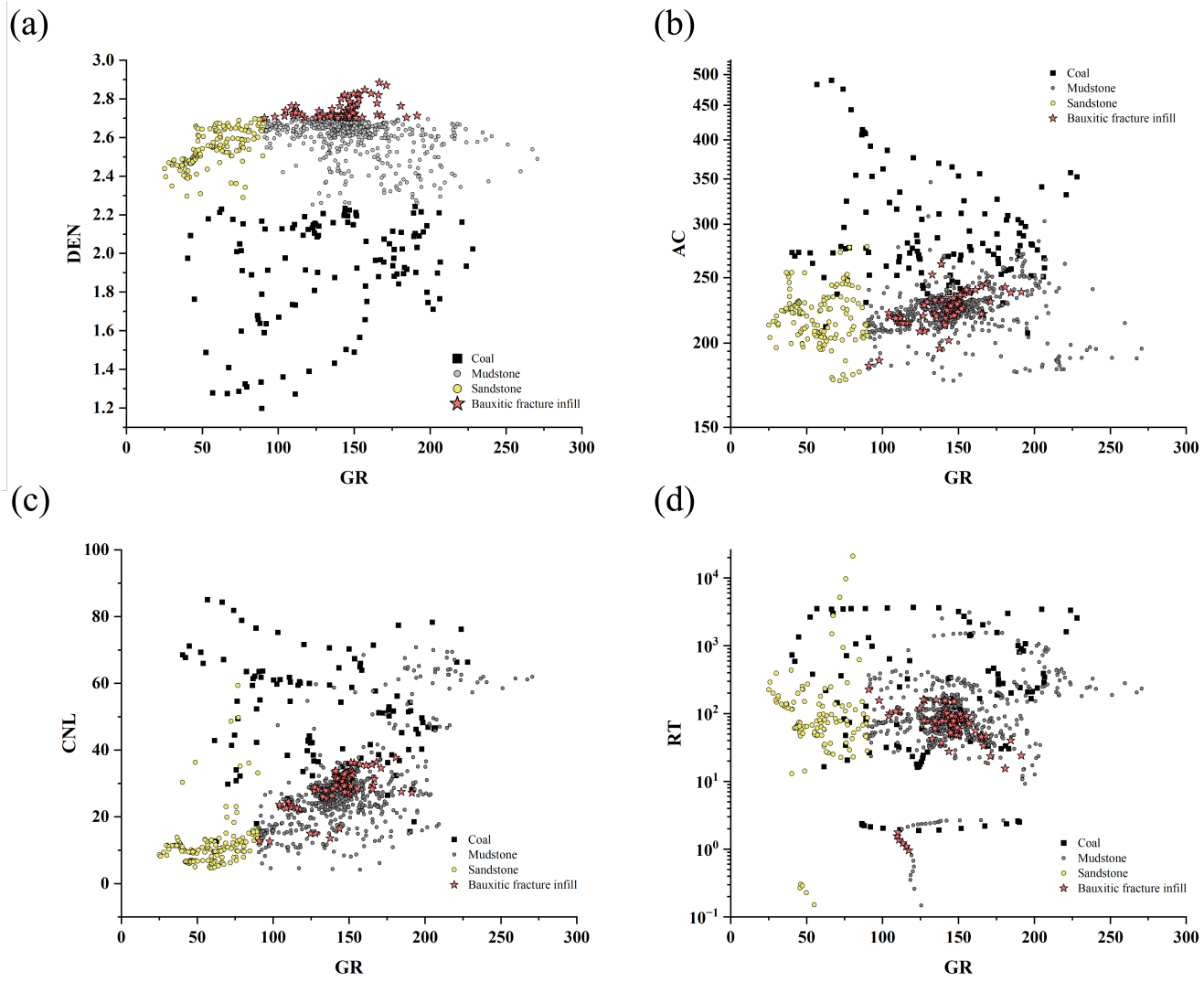


Figure 9. Logging Data intersection diagram; (**a**) Intersection diagram of DEN and GR; (**b**) Intersection diagram of AC and GR; (**c**) Intersection diagram of CNL and GR; (**d**) Intersection diagram of RT and GR.

7. Impact on Reservoir Seepage and Accumulation

Fractures are the "lifeline" of tight gas reservoirs, and their effectiveness is strongly controlled by the fracture-filling degree. This section explores the dual role of aluminous fracture filling on reservoir seepage behavior based on permeability experiments conducted on naturally fractured core samples.

7.1. Magnitude Differences in Permeability Evolution

Overburden permeability tests were performed on core samples containing natural fractures developed within the bauxite series reservoirs. For fractured cores, paired measurements were conducted on both the fractured interval and the adjacent intact matrix to distinguish fracture-controlled permeability from matrix permeability under the same lithological background. The experimental dataset includes matrix samples without visible fractures ($n = 36$), natural fractures without mineral filling ($n = 21$), and natural fractures partially to extensively filled with Al–Si colloidal materials ($n = 21$).

The permeability evolution characteristics of different fracture states are summarized in Figure 10:

Open fractures: Permeability is extremely high (10^2–$10^5 \times 10^{-3}$ μm^2), representing highly efficient migration pathways. However, these fractures exhibit strong stress sensitivity, and permeability decreases sharply with increasing confining pressure.

Aluminous-filled fractures (partially filled): Permeability ranges from 10^1 to $10^4 \times 10^{-3}$ μm^2. Compared with open fractures, permeability is reduced by approximately one to two orders of magnitude due to partial occlusion by aluminous mineral fillings.

Matrix: Permeability is typically lower than 1×10^{-3} μm^2, reflecting the intrinsically tight nature of the host rock.

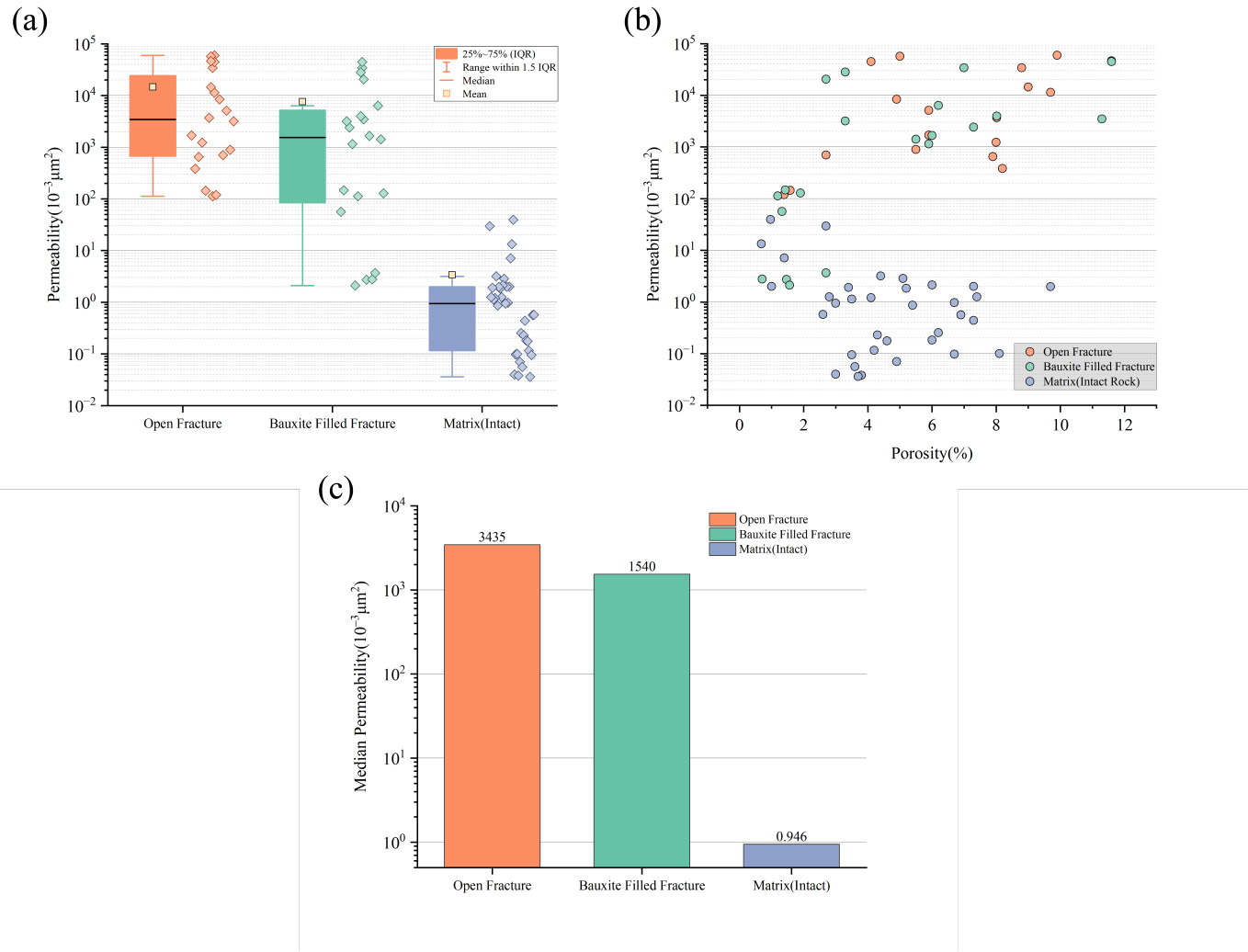


Figure 10. Permeability characteristics of samples with different fracture states: (**a**) boxplots of permeability for open fractures, bauxite-filled fractures, and intact matrix samples, with outliers retained to reflect natural fracture heterogeneity; (**b**) permeability–porosity crossplots illustrating the distinct clustering behavior of different fracture states; (**c**) comparison of median permeability values for each fracture category. All individual permeability measurements are shown; no statistical outliers were excluded from the dataset.

It should be noted that several high- and low-permeability outliers are present in the boxplot distributions (Figure 10a). These outliers were not removed, as they represent natural heterogeneity inherent to fracture-controlled permeability systems. In particular, unusually high permeability values in the open-fracture and partially filled fracture groups likely correspond to locally wider apertures or better-connected fracture segments, whereas low-permeability outliers may reflect partial clogging, mineral overgrowth, or

localized stress effects. Importantly, the presence of these outliers does not alter the overall permeability hierarchy or the order-of-magnitude contrasts among fracture states.

Although aluminous mineral filling reduces fracture permeability, aluminous-filled fractures remain three to four orders of magnitude more permeable than the surrounding matrix. The paired measurement approach demonstrates that even partially blocked natural fractures can function as relatively high-permeability channels in tight reservoirs, providing effective pathways for gas migration and supporting the proposed bypass gas supply mechanism.

7.2. Propping and Anti-Compaction Effects

Stress sensitivity experiments show that permeability decay with increasing confining pressure is significantly slower in aluminous-filled fractures than in open ones. Hard diaspore and dense colloids act as natural "proppants," preventing complete closure under deep burial high pressure. This propping effect maintains residual aperture at depths >3000 m, a key factor for deep tight gas accumulation [57].

7.3. "Bypass Supply" Migration Model

By integrating fracture-scale microstructural observations with seepage experimental results, a conceptual model for gas migration and accumulation in aluminous fracture systems is proposed (Figure 11). The model illustrates the progressive evolution of fracture function from fluid conduit to composite storage–transport system.

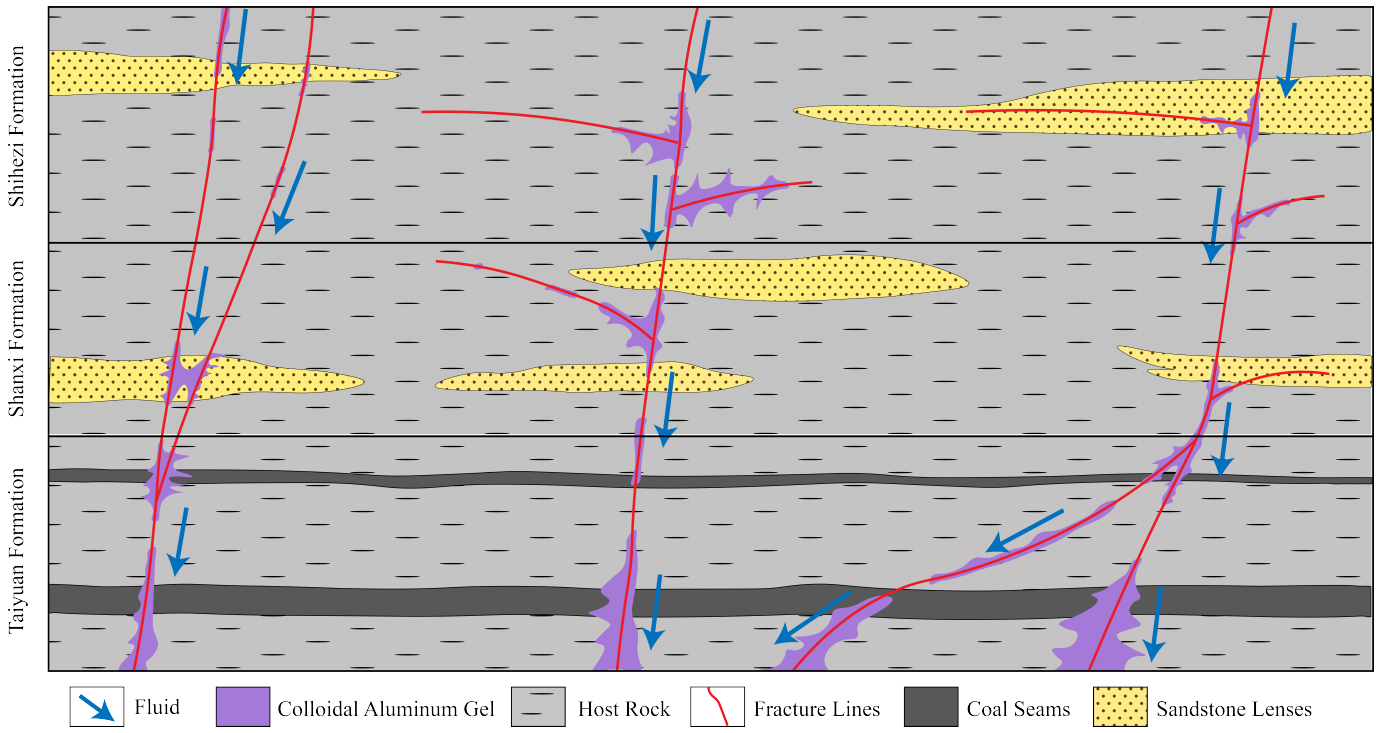


Figure 11. Conceptual model illustrating the multistage evolution of aluminous fracture filling and its role in gas migration and accumulation. The model depicts the transition from early open fractures acting as fluid conduits, through intermediate-stage segmented and tortuous flow systems formed by Al–Si colloidal fracture fillings, to late-stage composite accumulation characterized by matrix supply, fracture transport, and gas retention within mineral-filled fracture networks ("bypass gas supply" mechanism).

During the early stage (charge stage), fractures are initially open and act as effective pathways for acidic fluid migration. Water–rock interaction promotes mineral dissolution

and initiates aluminous precipitation along fracture walls, while fracture conductivity remains high [58].

In the middle stage (modification stage), continued aluminous mineral precipitation leads to the development of globular and plug-like fillings, which segment originally continuous fractures into a complex "network–vug" system. Although overall fracture permeability is reduced, fluids are redirected to flow around mineral fillings along tortuous pathways, increasing fluid–matrix contact and enhancing interaction between fractures and the surrounding rock.

In the late stage (accumulation stage), gas charging becomes dominant. Al–Si colloidal fracture fillings partially restrict direct gas flow but simultaneously provide micro- to nanoscale intercrystalline pore systems with high capillary forces capable of retaining gas. Importantly, residual vermicular or unblocked micro-channels within the filled fractures remain hydraulically connected to matrix pores, forming an integrated "matrix supply–fracture transport–filling retention" accumulation system. This bypass gas supply mechanism enables efficient gas migration and storage even in intervals that appear macroscopically tight, thereby explaining the high gas productivity observed in aluminous bauxite reservoirs.

8. Conclusions

Based on a comprehensive study of the petrological, geochemical, logging, and seepage characteristics of fractures in aluminum-bearing rock series in the Ordos Basin, this report draws the following main conclusions.

Fracture fillings have unique markers and evolutionary sequences. Fillings are mainly amorphous aluminosilicate gel, gibbsite, kaolinite, and late diaspore/illite. Amorphous colloids' optical features (fully dark under XPL, uniform pink under λ plate) identify early rapid filling. The morphology evolves: "Wall-lining film $\rightarrow$ Oolitic/Globular $\rightarrow$ Plug-like $\rightarrow$ Vermicular," recording the transition from open conduits to complex pore networks. Globule drag direction indicates paleo-fluid paths.

The *pH-Eh* evolution of the water–rock reaction is the geochemical core of the precipitation of aluminum minerals. Geochemical simulations indicate that acidic formation water (at temperatures exceeding 120 °C) can enhance feldspar leaching, promoting an increase in *pH* and a decrease in *Eh* that favor the dehydration and crystallization of Al–Si colloids, and facilitating the kaolinite-to-illite transformation. These results suggest that the filling evolution is primarily governed by thermodynamic driving forces.

The logging identification model of "three highs and two lows". Aluminum fracture-filling bands exhibit typical characteristics in logging, such as high natural gamma (120–200 API), high density (2.55–2.75 g/cm^3), high neutron porosity (15–25 p.u.), low acoustic time difference (190–220 μs/m), and low resistivity. Based on the intersection map of GR–DEN and GR–AC, the interference of surrounding rock can be effectively eliminated, and the rapid identification of aluminum fracture zones in the wellbore profile can be achieved.

Aluminum filling exerts a dual positive effect of both "blocking" and "supporting" on tight gas accumulation. Although Al–Si colloidal fracture fillings reduce fracture permeability by 1–2 orders of magnitude relative to open fractures, the retained permeability remains 3–4 orders of magnitude higher than that of the matrix, allowing fractures to continue functioning as dominant flow conduits. More importantly, the dense Al–Si colloidal fracture fillings act as a natural proppant-like framework, significantly reducing fracture stress sensitivity and helping to preserve seepage capacity under deep burial conditions. Meanwhile, their complex micro- to nanoscale pore structures facilitate fluid bypass around

partially filled segments, forming a distinctive "bypass gas supply" network that promotes gas retention and accumulation within the bauxite rock series.

9. Discussion

Beyond the Ordos Basin, the fracture-filling mechanisms and diagnostic criteria proposed in this study are expected to be applicable to other leaching-affected lithological systems in sedimentary basins. In such systems, fluid-driven *pH-Eh* evolution, colloid-mediated mineral precipitation, and fracture-controlled fluid pathways may similarly govern fracture filling, seepage behavior, and gas accumulation, providing a transferable framework for reservoir evaluation under comparable diagenetic conditions.

Mineralogical compositions were constrained using standard X-ray diffraction (XRD) quantification (Table 1), which primarily resolves crystalline clay minerals such as illite, kaolinite, chlorite, and illite/smectite mixed layers. It should be noted that standard bulk XRD protocols are inherently more sensitive to well-crystallized phases, whereas amorphous to poorly crystalline Al–Si materials inferred from petrographic observations may not be readily detected due to their limited long-range crystallographic order and potentially low abundance. Future work combining TEM or synchrotron-based techniques could further constrain nanoscale phase evolution.

Consequently, the occurrence of early-stage gel-like Al–Si colloidal materials is interpreted mainly based on integrated petrographic characteristics, textural context, and geochemical constraints. While complementary techniques such as electron microscopy could further refine the mineralogical characterization of these materials, the current integrated approach is sufficient to establish their role in fracture filling and diagenetic evolution.

Author Contributions: Conceptualization, J.Z.; Methodology, H.Z. and J.Z.; Software, H.Z.; Validation, H.Z.; Formal Analysis, H.Z.; Investigation, H.Z.; Resources, J.Z.; Data Curation, H.Z.; Writing—Original Draft Preparation, H.Z.; Writing—Review and Editing, H.Z.; Visualization, H.Z.; Supervision, J.Z.; Project Administration, J.Z.; Funding Acquisition, J.Z. All authors have read and agreed to the published version of the manuscript.

Funding: This work was supported by the project "Helium Enrichment and Detection in Natural Gas Reservoirs Related to Oil and Gas Fields" (Grant No. 2025ZD1010500), as part of the "Deep Earth Probe and Mineral Resources Exploration–National Science and Technology Major Project".

Institutional Review Board Statement: Not applicable.

Informed Consent Statement: Not applicable.

Data Availability Statement: The data presented in this study, including core images and thin-section micrographs, are available on request from the corresponding author. The raw well logging and production data are not publicly available due to privacy and proprietary restrictions associated with PetroChina Changqing Oilfield Company.

Acknowledgments: The authors would like to express their gratitude to the Research Institute of Exploration and Development, PetroChina Changqing Oilfield Company, for providing the core samples and geological data (Wells Yu 27, Su 76, Su 116, Su 121, Shan 211, Shan 329) essential for this study. We also extend our appreciation to the Petroleum Geology Testing Center of the Geological Scientific Research Institute of Shengli Oilfield Company, SINOPEC, for their assistance with the permeability and stress sensitivity testing.

Conflicts of Interest: The authors declare no conflict of interest. The funders had no role in the design of the study; in the collection, analyses, or interpretation of data; in the writing of the manuscript; or in the decision to publish the results.

References

1. Yang, S.; Wang, Q.; Xu, L.; Qin, R.; Ma, H.; Chen, F. Lithium enrichment in karst bauxitic sequences: A case study from the Youjiang Basin, South China. *Geol. Soc. Am. Bull.* **2025**, *in press*. [CrossRef]
2. Wang, W.; Sun, X.; Liu, L.; Zhao, L.; Liang, R.; Zhang, T.; Liu, X. Metallogenic process of forming the large xiangcaowa karstic bauxite deposit from the southern margin of the North China craton. *Minerals* **2025**, *15*, 310. [CrossRef]
3. Thomassen, G.; Eswaran, A.; Van Passel, S.; Dewulf, J. A planetary boundary for mineral, metal, and fossil resource extraction rates: How much primary materials can a circular economy extract? *Environ. Sci. Technol.* **2024**, *58*, 20345–20351. [CrossRef]
4. Kronyak, R.E.; Kah, L.C.; Edgett, K.S.; VanBommel, S.J.; Thompson, L.M.; Wiens, R.C.; Sun, V.Z.; Nachon, M. Mineral-filled fractures as indicators of multigenerational fluid flow in the Pahrump Hills member of the Murray Formation, Gale Crater, Mars. *Earth Space Sci.* **2019**, *6*, 238–265. [CrossRef]
5. Liu, X.; Wang, Q.; Peng, Y.; Yin, R.; Ma, Y.; Zhao, L.; Zhang, S. Intensified and apace bauxitization over the paleo-karstic surface linked to volcanism. *GSA Bull.* **2022**, *135*, 1187–1205. [CrossRef]
6. Li, X.; Chen, G.; Shi, J.; Song, P.; Liu, J.; Sun, D.; Wang, D. Ancient-present tectonic differences and evolution characteristics of the Meso-Neoproterozoic in the southern Ordos Basin. *Geol. Mag.* **2025**, *162*, e32. [CrossRef]
7. Lv, D.; Shen, Y.; van Loon, A.J.T.; Raji, M.; Zhang, Z.; Song, G.; Ren, Z.; Wang, Y.; Wang, D. Sequence stratigraphy of the Middle Jurassic Yan'an formation (NE Ordos Basin, China), relationship with climate conditions and basin evolution, and coal maceral's characteristics. *Front. Earth Sci.* **2023**, *10*, 1086298. [CrossRef]
8. Li, H.; Fu, J.; Ji, H.; Zhang, L.; She, Y.; Guan, W.; Jing, X.; Wang, H.; Cao, Q.; Liu, G.; et al. Bauxite series in the Upper Paleozoic weathering crusts in the southwestern Ordos Basin: Development and distribution of dominant reservoirs. *Oil Gas Geol.* **2023**, *44*, 1243–1255. Available online: https://www.sciopen.com/local/article_pdf/10.11743/ogg20230513.pdf (accessed on 1 November 2023).
9. dos Santos Albuquerque, M.F.; Horbe, A.M.C.; Gautheron, C.; Vieira, J.G.C.; Val, P.; Pinna-Jamme, R.; Salazar, C.A. (UTh)/he geochronology of fe and FeAl lateritic duricrusts and bauxites in Central-Northern Amazonia: Implications for paleoclimate and landscape evolution. *Chem. Geol.* **2025**, *689*, 122835. [CrossRef]
10. Yu, S.; Zhao, Z.; Zhu, Y.; Zhu, X.; Lai, J.; Li, D.; Wang, X. Reservoir characteristics and formation model of the bauxite gas reservoir: The benxi formation in the LX block, northeast of Ordos Basin, China. *ACS Omega* **2024**, *9*, 18127–18136. [CrossRef]
11. Li, Y.; Gao, X.; Meng, S.; Wu, P.; Niu, X.; Qiao, P.; Elsworth, D. Diagenetic sequences of continuously deposited tight sandstones in various environments: A case study from Upper Paleozoic sandstones in the Linxing area, eastern Ordos Basin, China. *AAPG Bull.* **2019**, *103*, 2757–2783. [CrossRef]
12. Feng, M.; Liu, T.; Lin, T.; Liu, X.; Li, N.; Xi, A. Fracture fillings and implication of fluid activities in volcanic rocks: Dixi area in Kelameili gas field, Junggar Basin, northwestern China. *Minerals* **2019**, *9*, 154. [CrossRef]
13. Liu, N.; Nan, J.; Wang, X.; Yang, Y.; Yin, P.; Zhang, R. Petrological characteristics and rock nomenclature of sedimentary bauxite gas reservoir: A case study of bauxite in Taiyuan formation of Ordos Basin. *Geofluids* **2023**, *2023*, 7079959. [CrossRef]
14. Ning, F.; Lin, H.; Zhou, C.; Yun, J.; Li, P.; Song, H. Characteristics of strike-slip fault-related reservoirs and the significance for hydrocarbon accumulation in the central Tarim Basin: Insights from the modern karst model. *Front. Earth Sci.* **2022**, *10*, 987020. [CrossRef]
15. Mitchell, S.F.; Ball, J.D.; Crowley, S.F.; Marshall, J.D.; Paul, C.R.C.; Veltkamp, C.J.; Samir, A. Isotope data from cretaceous chalks and foraminifera: Environmental or diagenetic signals? *Geology* **1997**, *25*, 691–694. [CrossRef]
16. Idriss, I.M. Finite element analysis for the seismic response of earth banks. *J. Soil Mech. Found. Div.* **1968**, *94*, 617–636. [CrossRef]
17. Lawley, C.J.; Petts, D.C.; Lee, W.S.; Brueckner, S. Pyrite geochemistry for deposit type prediction and exploration in the Golden Triangle, northwest British Columbia, Canada. *Ore Geol. Rev.* **2025**, *177*, 106447. [CrossRef]
18. Luo, A.B.; Wang, M.; Zeng, X.W.; Hao, Y.J.; Li, H. An extensional collapse model for the Lhasa–Qiangtang orogen in Central Tibet. *Gondwana Res.* **2021**, *89*, 66–87. [CrossRef]
19. Xu, J.J.; Cheng, X.G.; Peng, S.N.; Jiang, J.C.; Wu, Q.L.; Lou, D.; Cheng, F.Q.; Lin, L.M. Differences and identification on multi-time hydrocarbon generation of carboniferous-permian coaly source rocks in the Huanghua Depression, Bohai Bay Basin. *Pet. Sci.* **2024**, *21*, 765–776. [CrossRef]
20. Sun, F.; Qu, C.; Cao, G.; Xie, L.; Shi, X.; Luo, S.; Liu, Z.; Zhang, L.; Ma, X.; Zhou, X.; et al. Oolitic sedimentary characteristics of the Upper Paleozoic bauxite series in the eastern Ordos Basin and its significance for oil and gas reservoirs. *Processes* **2024**, *12*, 2123. [CrossRef]
21. Zhang, Z.; Dai, J.; Wang, X.; Hu, Z.; Wan, X.; Peng, B.; Fu, M. Application of spectroscopic characteristics of white mica in porphyry tungsten deposits: A case study involving the Shimensi deposit in northern Jiangxi. *Minerals* **2023**, *13*, 256. [CrossRef]
22. Gountié Dedzo, M.; Klamadji, M.N.; Zangmo Tefogoum, G.; Chako-Tchamabé, B.; Asaah, A.N.E.; Tchameni, R. Major, trace elements and sr–nd–pb isotopes systematics of mafic dykes from the figuil (northern Cameroon) and léré (southwestern Chad) areas. *Geol. J.* **2024**, *59*, 784–810. [CrossRef]

23. Li, Y.; Wang, Z.; Shao, L.; Gong, J.; Wu, P. Reservoir characteristics and formation model of Upper Carboniferous bauxite series in eastern Ordos Basin, NW China. *Pet. Explor. Dev.* **2024**, *51*, 44–53. [CrossRef]
24. English, J.; Laubach, S. Opening-mode fracture systems: Insights from recent fluid inclusion microthermometry studies of crack-seal fracture cements. *Geol. Soc. Lond. Spec. Publ.* **2017**, *458*, 257–272. [CrossRef]
25. Hikmet Kinaci, E.; Ozturk, A. Gemological features of diaspore in Sodra—Milas (Mugla) region. *Front. Earth Sci.* **2023**, *11*, 1145674. [CrossRef]
26. Huang, P.; Liu, M.J.; Cao, B.; Wang, Z.L. Diagenesis and implication for the reservoir quality of the tight sandstone reservoir in the depression zone of foreland basin, Upper Triassic Xujiahe Formation, Western Sichuan Foreland Basin, China: Evidence from petrography and geochemistry. *Pet. Sci.* **2025**, *22*, 102016. [CrossRef]
27. Spielman-Sun, E.; Boye, K.; Dwivedi, D.; Engel, M.; Thompson, A.; Kumar, N.; Noël, V. A critical look at colloid generation, stability, and transport in redox-dynamic environments: Challenges and perspectives. *ACS Earth Space Chem.* **2024**, *8*, 630–653. [CrossRef]
28. Zhang, S.; Li, X.; Lan, J.; Lin, C.; Zhang, D.; Duan, H. Impact of clay minerals on oil displacement efficiency in tight oil reservoirs. *Arab. J. Chem.* **2026**, *19*, 3372025. [CrossRef]
29. Wu, X.; Chen, Z.; Shen, Z.; Bao, Y.; Lan, Z.; Liu, P.; Dou, L.; Wen, Z. Lithofacies controls on gas accumulation in tight sandstone reservoirs: Insights from the Permian Shihezi formation, south-western ordos basin, china. *Front. Earth Sci.* **2025**, *13*, 1610578. [CrossRef]
30. Qi, Y.; Li, D.; Yu, S.; Li, Q. Geophysical exploration methods on bauxite reservoirs in L gasfield, Ordos Basin. *Front. Energy Res.* **2023**, *11*, 1328662. [CrossRef]
31. Zhang, P.; Jing, X.; Pu, R.; Wang, A.; Huang, X. Logging identification and distribution of bauxite in the southwest Ordos Basin. *Minerals* **2023**, *13*, 1253. [CrossRef]
32. Wang, R.; Wang, Q.; Huang, Y.; Yang, S.; Liu, X.; Zhou, Q. Combined tectonic and paleogeographic controls on the genesis of bauxite in the Early Carboniferous to Permian Central Yangtze Island. *Ore Geol. Rev.* **2018**, *101*, 468–480. [CrossRef]
33. Jiang, L.; Qiu, Z.; Wang, Q.; Guo, Y.; Wu, C.; Wu, Z.; Xue, Z. Joint development and tectonic stress field evolution in the southeastern Mesozoic Ordos Basin, west part of North China. *J. Asian Earth Sci.* **2016**, *127*, 47–62. [CrossRef]
34. He, T.; Zhou, Y.; Li, Y.; Zhang, Z.; Zhang, Y.; Cui, G. The tectonic-sedimentary evolution of the Yan'an formation in the Ordos Basin and its petroleum geological significance. *Appl. Sci.* **2024**, *14*, 9278. [CrossRef]
35. Wang, R.; Shi, W.; Xie, X.; Zhang, W.; Qin, S.; Liu, K.; Busbey, A. Clay mineral content, type, and their effects on pore throat structure and reservoir properties: Insight from the Permian tight sandstones in the Hangjinqi area, north Ordos Basin, China. *Mar. Pet. Geol.* **2020**, *115*, 104281. [CrossRef]
36. Huang, W.L. Stability and kinetics of kaolinite to boehmite conversion under hydrothermal conditions. *Chem. Geol.* **1993**, *105*, 197–214. [CrossRef]
37. Jiang, F.; Jia, C.; Pang, X.; Jiang, L.; Zhang, C.; Ma, X.; Qi, Z.; Chen, J.; Pang, H.; Hu, T.; et al. Upper Paleozoic total petroleum system and geological model of natural gas enrichment in Ordos Basin, NW China. *Pet. Explor. Dev.* **2023**, *50*, 281–292. [CrossRef]
38. Wang, Y.; Guo, J.; Ma, Z.; Zhou, L. Rapid identification of an effective bauxite gas reservoir by principal component analysis. *Sci. Rep.* **2024**, *14*, 23466. [CrossRef] [PubMed]
39. He, J.; Li, S.; Zhao, A.; Wang, D.; Gao, J.; Zhou, X.; Ahmed, M.S.; Wang, Z.; Zhu, L. The relationship between helium-rich gas and regional shale in the sichuan basin, southwest China. *Front. Earth Sci.* **2024**, *12*, 1491017. [CrossRef]
40. Li, J.; Dai, C.; Lei, H. The influence of thermal boundary conditions of wellbore on the heat extraction performance of deep borehole heat exchangers. *Geothermics* **2022**, *100*, 102325. [CrossRef]
41. Xu, G.; Zhang, L.; Pang, X.; Chen, M.; Xu, S.; Liu, B.; Zuo, Y.; Luo, S.; Hu, L.; Chen, H.; et al. New method for the reconstruction of sedimentary systems including lithofacies, environments, and flow paths: A case study of the Xisha Trough Basin, South China Sea. *Mar. Pet. Geol.* **2021**, *133*, 105268. [CrossRef]
42. Huang, W.; Xi, K.; Cao, Y.; Shan, X.; Cui, Z.; Hellevang, H. Mechanisms of feldspar dissolution and associated authigenic mineral precipitation in coal measure tight sandstone reservoirs: Insights using a reaction-transport numerical model incorporating organic chelation. *Adv. Geo-Energy Res.* **2025**, *18*, 51–68. [CrossRef]
43. Hu, S.; Li, D.; Li, Y.; Guo, Q.; Tian, D.; Zhang, L.; Li, H. Preparation of foamed ceramics from graphite tailings using a self-foaming method. *Minerals* **2023**, *13*, 521. [CrossRef]
44. Dai, W.; Moynier, F.; Paquet, M.; Moureau, J.; Debret, B.; Siebert, J.; Gerard, Y.; Zhao, Y. Calcium isotope measurements using a collision cell (CC)-MC-ICP-MS. *Chem. Geol.* **2022**, *590*, 120688. [CrossRef]
45. Wu, S.; Zhang, Y.; Zhang, Y.; Gong, Y.; Hao, Z. Preparation and characterization of kaolinite supported lanthanum-hydroxide and its improvements for natural rubber composites. *Appl. Clay Sci.* **2022**, *216*, 106342. [CrossRef]
46. Balabantaray, S.K.; Aravindan, S.; Ravi, R. Morphological, microstructural and mineralogical dataset of bauxite over Mainpat plateau from a part of Deccan traps, Surguja district, Chhattisgarh. *SN Appl. Sci.* **2020**, *2*, 1897. [CrossRef]
47. Earle, S. 5.2 chemical weathering. In *Physical Geology*, 2nd ed.; BCcampus: Vancouver, BC, Canada, 2019.

48. Cox, S.F. Antitaxial crack-seal vein microstructures and their relationship to displacement paths. *J. Struct. Geol.* **1987**, *9*, 779–787. [CrossRef]
49. Bons, P.D. The formation of veins and their microstructures. *J. Virtual Explor.* **2000**, *2*, 12. [CrossRef]
50. Spruženiece, L.; Späth, M.; Urai, J.L.; Ukar, E.; Selzer, M.; Nestler, B. Wide-blocky veins explained by dependency of crystal growth rate on fracture surface type: Insights from phase-field modeling. *Geology* **2021**, *49*, 641–646. [CrossRef]
51. Parkhurst, D.L.; Appelo, C.A.J. Description of input and examples for PHREEQC version 3: A computer program for speciation, batch-reaction, one-dimensional transport, and inverse geochemical calculations. In *Techniques and Methods*; Technical Report 6-A43; U.S. Geological Survey: Denver, CO, USA, 2013. [CrossRef]
52. Kotarba, M.J.; Słowakiewicz, M.; Misz-Kennan, M.; Więcław, D.; Jurek, K.; Waliczek, M. Simulated maturation by hydrous pyrolysis of bituminous coals and carbonaceous shales from the Upper Silesian and Lublin Basins (Poland): induced compositional variations in biomarkers, carbon isotopes and macerals. *Int. J. Coal Geol.* **2021**, *247*, 103856. [CrossRef]
53. Kelemen, Z.; Gillikin, D.P.; Borges, A.V.; Tambwe, E.; Sembaito, A.T.; Mambo, T.; Wabakhangazi, J.N.; Yambélé, A.; Stroobandt, Y.; Bouillon, S. Freshwater bivalve shells as hydrologic archives in the Congo basin. *Geochim. Cosmochim. Acta* **2021**, *308*, 101–117. [CrossRef]
54. Velderrain-Rojas, L.A.; Vidal-Solano, J.R. Middle-late miocene rift-related magmatism in Guaymas, Sonora, Mexico at the eastern margin of the Gulf of California: Petrogenetic implications associated to the Pacific-north American plate boundary. *Appl. Geochem.* **2023**, *148*, 105508. [CrossRef]
55. Smith, M.M.; Dai, Z.; Carroll, S.A. Illite dissolution kinetics from 100 to 280 °C and pH 3 to 9. *Geochim. Cosmochim. Acta* **2017**, *209*, 9–23. [CrossRef]
56. Wang, L.; Yang, Z.; Wei, B.; Zhao, Y.; Li, A.; Fu, X. Helium-generating potential evaluation of bauxite in Linxing area based on natural gamma-ray spectral logging. *World Geol.* **2024**, *43*, 557–565.
57. Witherspoon, P.A.; Wang, J.S.Y.; Iwai, K.; Gale, J.E. Validity of cubic law for fluid flow in a deformable rock fracture. *Water Resour. Res.* **1980**, *16*, 1016–1024. [CrossRef]
58. Liu, X.; Wang, Q.; Feng, Y.; Li, Z.; Cai, S. Genesis of the Guangou karstic bauxite deposit in western Henan, China. *Ore Geol. Rev.* **2013**, *55*, 162–175. [CrossRef]

Disclaimer/Publisher's Note: The statements, opinions and data contained in all publications are solely those of the individual author(s) and contributor(s) and not of MDPI and/or the editor(s). MDPI and/or the editor(s) disclaim responsibility for any injury to people or property resulting from any ideas, methods, instructions or products referred to in the content.